



Full Length Article

Effects of lateral swirl combustion chamber geometries on the combustion and emission characteristics of DI diesel engines and a matching method for the combustion chamber geometry

Xiangrong Li^{a,*}, Yanlin Chen^a, Liwang Su^b, Fushui Liu^a^a School of Mechanical Engineering, Beijing Institute of Technology, Beijing 100081, China^b China North Engine Research Institute (Tianjin), Tianjin 300400, China

ARTICLE INFO

Keywords:
 DI diesel engine
 Lateral swirl combustion system
 Geometry
 Optimization
 Matching method
 Combustion performance

ABSTRACT

Previous experimental results show that a lateral swirl combustion system (LSCS) significantly improves the fuel consumption and the soot emission in direct injection (DI) diesel engines. To further improve LSCS performance and effectiveness, this study undertook numerical simulation to analyze the effects of the LSCS chamber geometries on combustion and emission characteristics under the condition of 2500 r/min and full load, revealing the relevant influence mechanisms. Based on a sensitivity analysis on the indicated power, the chamber geometry optimization was accomplished. The performance improvement of the optimized LSCS was verified using a single-cylinder DI engine. However, due to the interplay between fuel spray jets and wall surfaces, the optimized results are different for various fuel supply systems. To apply the LSCS effectively in different fuel supply systems, a matching method for LSCS chamber geometry is proposed in this paper.

The results show that the combustion performance of the LSCS is primarily affected by the geometries of the split-flow creation, in which θ (the deviation angle of flow-guide) plays a dominant role. When θ was in the range of 15–27°, the combustion chamber created favorable flow guidance for spray and promoted the fuel/air mixture formation. After the geometrical optimization of the LSCS, fuel consumption decreased by 2.8–4.1 g/(kW.h) and soot emission decreased by 69–75% under various engine speeds as compared with the double swirl combustion system (DSCS).

1. Introduction

With ever-increasing injection pressures, direct injection (DI) diesel engines have become mainstream in diesel engines [1]. DI diesel engines are widely used in transportation, engineering and agricultural machinery due to the excellent dynamic performance and fuel economy [2]. In DI diesel engines, the key to effective fuel/air mixture formation and combustion is optimizing the fuel spray along with the combustion chamber geometry and the in-cylinder air flow [3]. Therefore, improving the combustion chamber geometry is an important component of enhancing combustion and emission performance [4].

In view of the interplay between the fuel spray and the combustion chamber, DI combustion systems can be divided into two types: the encompassing combustion system (ECS) and the wall-flow-guided combustion system (WFGCS). The ECS has a combustion chamber that can well-envelop the spray profile, including such systems as the traditional omega combustion system (OMECS), the dumbbell-shaped combustion system [5] and the toroidal re-entrant combustion chamber (TRCC) [6].

However, special combustion chamber geometry has been designed in the WFGCS to guide the fuel spray along an intended trajectory. The WFGCS includes such systems as the double swirl combustion system (DSCS) [7], the BUMP combustion system [8], the umbrella-curtain spray (UCS) combustion system [9] and the swirl chamber combustion system [10]. Under the high injection pressure condition, the spray ejected from the nozzle penetrated into the ambient gas of combustion chamber with high speed [11]. Owing to the high spray speed and small combustion chamber, the fuel spray might impinge on the piston wall before being fully vaporized in real DI diesel engines and “wall-wetting” problem appears, especially in downsized engines [12]. Wall-wetting mainly causes excessive soot emissions to the DI diesel engines [13]. Obviously, the spray impingement worsens the performance of diesel engines by altering the fuel mixing, combustion and emissions [14]. Therefore, the ECS has encountered difficulties in adapting to present fuel supply systems, while the aforementioned WFGCS shows great potential by utilizing special chamber geometry and injection energy to promote the formation and subsequent combustion of the fuel/air mixture.

* Corresponding author.

E-mail address: prof.lixr@yahoo.com (X. Li).

Nomenclature

| | |
|------------|-------------------------------------|
| DI | direct injection |
| LSCS | lateral swirl combustion systems |
| DSCS | double swirl combustion systems |
| OMECS | omega combustion systems |
| ECS | encompassing combustion systems |
| WFGCS | wall-flow-guided combustion systems |
| r_t | central boss radius |
| δ_t | inclination angle of central boss |
| h_t | central boss depth |
| r_c | connective arc radius |

| | |
|--------------------|--|
| β | radius angle of the combustion chamber |
| D | combustion chamber diameter |
| h_a | convex edge height |
| r_a | split arc radius |
| TDC | top dead center |
| BDC | bottom dead center |
| FS | full scale |
| FSN | filter smoke number |
| FSO | full-scale output |
| P_i | indicated power |
| θ | deviation angle of flow-guide |
| $h_{a,\text{opt}}$ | optimal convex edge height |

In a combustion chamber, the circumferential air zone can be divided into two parts: A and B, as shown in Fig. 1 [15]. In previous ECS and WFGCS chambers, the fuel/air mixture was mainly focused on zone A, while the air in zone B was not fully utilized unless an appropriate intake swirl was induced. However, the intake swirl causes a loss of intake flow and intake mass as well as subdue the effectiveness of the wall-flow-guide. To fully utilize the fuel injection energy and the air in zone B, a lateral swirl combustion system (LSCS) was developed as a new WFGCS [16]. Fig. 2 shows the schematic diagram of the LSCS. As compared with the OMECS, special split-flow creations are introduced in the LSCS, the number of which is 2 times the number of nozzle holes. Every split-flow creation contains a convex edge and two split arcs. After colliding with the convex edge, a fuel jet spray splits into two

scrolled parts, and lateral swirls form. In this way, the air utilization in zone B is increased, whereupon the mixing effectiveness of fuel and air is improved. Experimental results indicate that the flame spread space of the LSCS is obviously increased after the spray impingement as compared with the OMECS; meanwhile, the LSCS achieves better fuel consumption and less soot emission than the OMECS in test engines [17]. The LSCS also shows strong adaptability to the excess air coefficient and has satisfactory combustion performance under a low excess air ratio of 1.3. Furthermore, the thermal load of the cylinder head is low because the combustion occurs mainly in the bottom of the combustion chamber, and the convex edges will not be ablated in virtue of the cooling effects of the fuel spray jets [18].

Evidently, due to its unique fuel/air mixing method, the LSCS shows remarkable combustion performance as well as fuel economy and soot emission quality, demonstrating great research value and potential. As the core of the LSCS, the combustion chamber geometry has a significant effect on the combustion performance. Moreover, the wall-flow-guided effectiveness of the LSCS is closely related to the fuel injection energy, so it is of great importance to achieve an appropriate match between the LSCS chamber geometry and the fuel supply system. Simply put, the optimal LSCS chamber geometry varies in different fuel supply systems. However, previous LSCS chambers were designed primarily based on the OMECS chambers. Up until now, the effect of LSCS chamber geometry on combustion performance has not been studied, and the geometrical optimization of the LSCS chamber has not been conducted. As such, there is no effective matching method for LSCS chamber geometry, which greatly limits the practicability and applicability of the LSCS.

In this study, the effects of the LSCS chamber geometries on the combustion and emission characteristics of DI diesel engines were

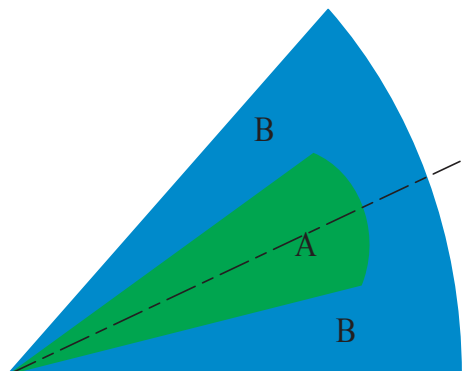


Fig. 1. Circumferential air zone in a combustion chamber.

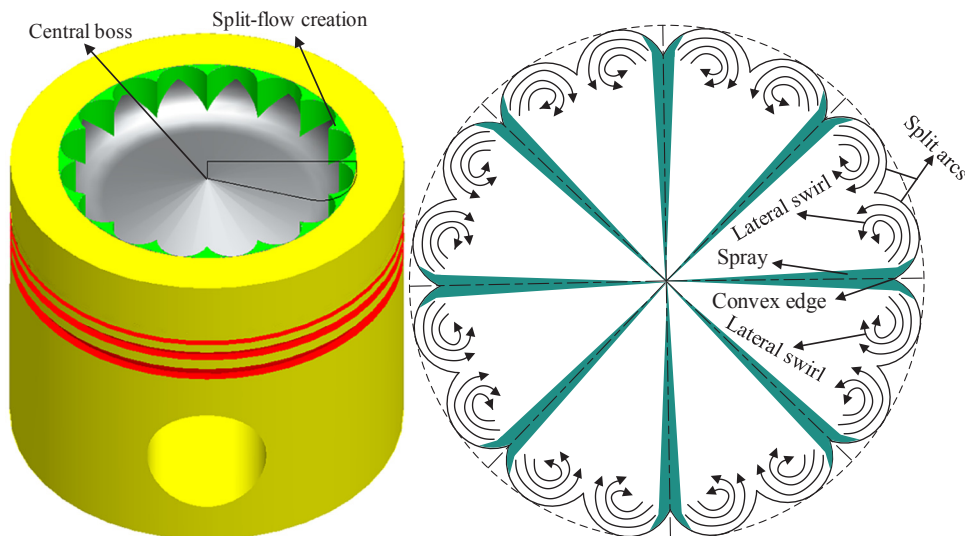


Fig. 2. Schematic diagram of the LSCS.

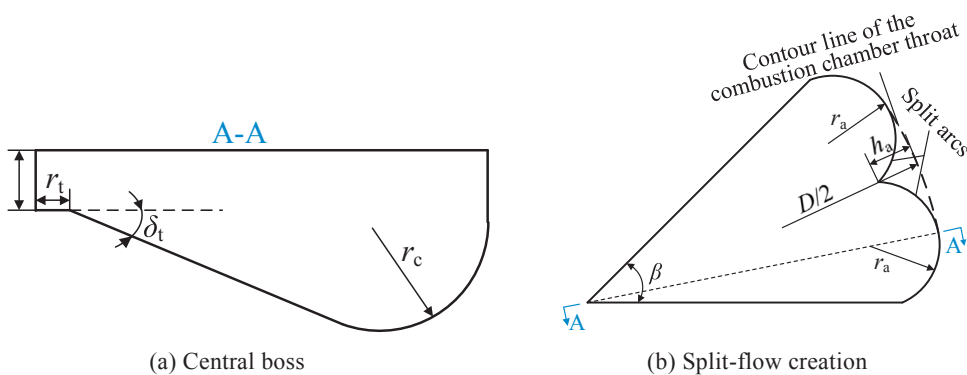


Fig. 3. Geometrical structure of the LSCS chambers.

analyzed by using AVL Fire under the condition of 2500 r/min and full load, which is the most noteworthy condition due to the difficult mixing of fuel and air. Additionally, the in-cylinder fuel/air equivalence ratio was studied to reveal the influence mechanisms of relevant geometries on the LSCS combustion performance. Then, the LSCS chamber geometry was optimized, and its performance was verified in a single-cylinder diesel engine. Furthermore, based on the above-mentioned study, a matching method for LSCS chamber geometry was developed and is proposed in this paper. The research results provide a sound reference for optimizing combustion systems, promoting fuel/air mixing, improving combustion processes and reducing soot emission in DI diesel engines.

2. Analytical methodology

2.1. Combustion chamber parameterization

The geometrical structure of the LSCS chambers includes two parts: the central boss and the split-flow creation. The central boss geometries include the central boss radius r_t , the inclination angle of central boss δ_t , the central boss depth h_t and the connective arc radius r_c , as shown in Fig. 3(a). The core of the combustion chamber is the split-flow creation, the geometries of which include the combustion chamber diameter D , the convex edge height h_a , and the split arc radius r_a , as shown in Fig. 3(b). D affects the distance that spray travels from the nozzle hole to the convex edge, which is described as the strength of spray impingement. h_a affects the strength and direction of spray impingement. r_a affects the development of the lateral swirls. Additionally, β is the radius angle of the combustion chamber, the value of which is related to the number of nozzle holes. In this study, a fuel injector with eight nozzle holes was adopted, so the value of β was 45°.

If D and h_a are certain, then r_a will be uniquely determined as:

$$r_a = \frac{D\left(1-\cos\frac{\beta}{4}\right)(D-2h_a) + 2h_a^2}{2D\left(1-\cos\frac{\beta}{4}\right) + 4h_a\cos\frac{\beta}{4}} \quad (1)$$

The range of h_a is restricted by the geometrical structure, where the split arcs are tangent to the contour line of the combustion chamber throat. If D is certain, then two extrema of h_a will exist. When h_a is 0, the LSCS is equivalent to the OMECS; when the value of h_a reaches a maximum, all split arcs are externally tangent to each other. Therefore, the range of h_a is determined as:

Table 1
Basic parameters of the single-cylinder diesel engine.

| | |
|----------------------------|------|
| Rated speed (r/min) | 2500 |
| Bore (mm) | 132 |
| Stroke (mm) | 145 |
| Compression ratio (-) | 13.5 |
| Connecting rod length (mm) | 262 |
| Clearance (mm) | 2.5 |

$$h_a \in \left[0, \frac{D + D\left(\sin\frac{\beta}{4} - \cos\frac{\beta}{4}\right)}{2 + 2\sin\frac{\beta}{4}} \right] \quad (2)$$

2.2. Numerical study

Numerical models of the LSCS chambers were built based on a 132-mm single-cylinder diesel engine, the basic parameters of which are listed in Table 1. Table 2 lists the main parameters of the simulation. For the sub-model options provided by AVL Fire, $k-\epsilon$ model [19], Wave model [20], Dukowicz model [21], Eddy Breakup model [22], Kennedy/Hiroyasu/Magnussen model [23] and Heywood + temperature fluctuations model [24] were adopted, as listed in Table 3. The boundaries and initial conditions of the simulation are based on the

Table 2
Main parameters of the simulation.

| | |
|---|--------|
| Intake valve closure timing ('CA, ATDC) | -120.5 |
| Exhaust valve opening timing ('CA, ATDC) | 100 |
| In-cylinder pressure at intake valve closure (bar) | 5.26 |
| In-cylinder temperature at intake valve closure (K) | 401.3 |
| Fuel injection quantity (mg/nozzle hole) | 36 |
| Start/end of injection ('CA, ATDC) | -12/23 |
| Outlet diameter of nozzle hole (mm) | 0.27 |

Table 3
Sub-model options.

| | |
|---------------------|------------------------------------|
| Turbulence model | $k-\epsilon$ |
| Spray breakup model | Wave |
| Evaporation model | Dukowicz |
| Combustion model | Eddy Breakup |
| Soot model | Kennedy/Hiroyasu/Magnussen |
| NO model | Heywood + temperature fluctuations |

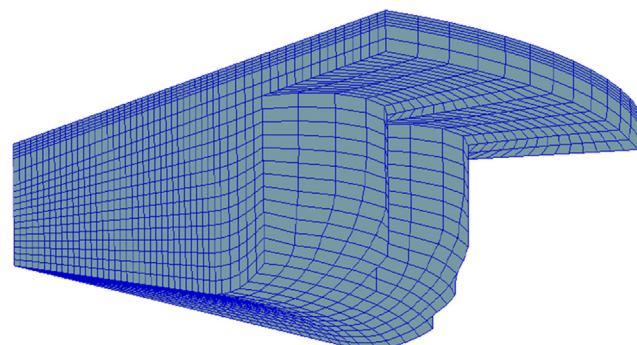


Fig. 4. Mesh specification of the LSCS chambers at TDC.

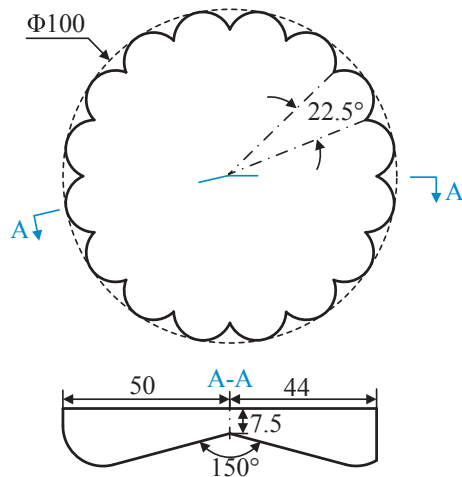


Fig. 5. Geometry of the reference chamber.

Table 4
The geometries of the reference combustion chamber.

| | | |
|--------------------------------|--|-----|
| Central boss geometries | Central boss radius r_c (mm) | 0 |
| | Inclination angle of central boss δ_t (°) | 15 |
| | Central boss depth h_c (mm) | 7.5 |
| | Connective arc radius r_c (mm) | 12 |
| Split-flow creation geometries | Combustion chamber diameter D (mm) | 100 |
| | Convex edge height h_a (mm) | 6 |

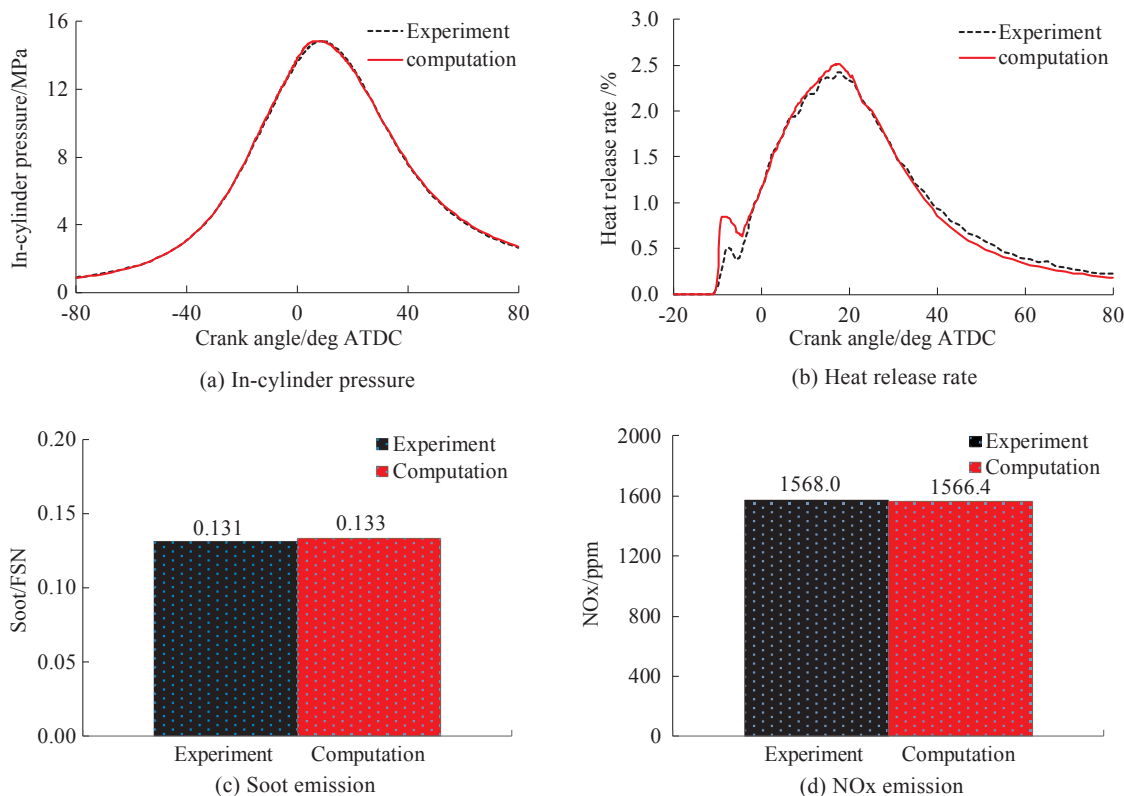


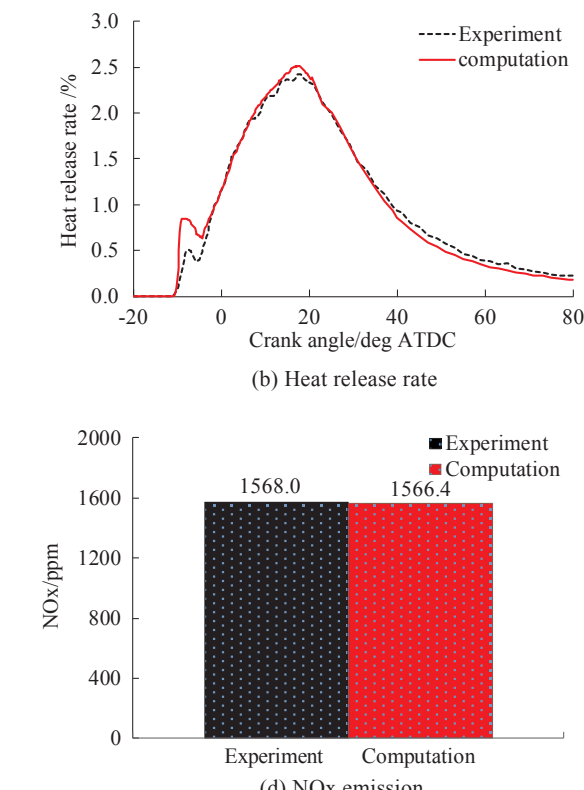
Fig. 6. Comparison of experimental and computational results.

experimental conditions in the test engine.

Because the nozzle holes and the LSCS chambers are circumferentially symmetric, only one-eighth of each chamber was modeled. To save computational resources, the models were simulated from the intake valve closure to the exhaust valve opening. To ensure the accuracy of simulation and reduce the calculation time, hexahedron meshes were chosen [25]. Considering the effect of mesh size on the simulation results, a proper value of mesh size was chosen to be 1 mm [26]. In this study, various LSCS chamber models were involved. To gain effective contrastive results, the volume, compression ratio and number of meshes were kept constant. The number of meshes at top dead center (TDC) and bottom dead center (BDC) was 10,860 and 20,760, respectively. Fig. 4 shows the mesh specification of the LSCS chambers at TDC.

In the numerical study, all LSCS chamber models were built based on a previous LSCS chamber, which was considered as the reference chamber. Fig. 5 shows the geometry of the reference chamber, the geometries of which are listed in Table 4.

To demonstrate the validity of the simulation, relevant tests were accomplished in the test engine. The speed and the brake power were 2500 r/min and 89 kW, respectively; the injection parameters were consistent with the simulating parameters listed in Table 2; the intake pressure was 350 kPa, and the excess air coefficient was 1.8. Then the experimental results of in-cylinder pressure, heat release rate, soot emission and NOx emission were used for model validation. Thereinto, the computational soot and NOx emission were derived from the in-cylinder calculating results at 100 °CA ATDC (exhaust valve opening timing), and the experimental results were measured in the exhaust pipe (as shown in Fig. 7). Moreover, numerical soot emission is characterized by a mass fraction, while the experimental result is characterized by filter smoke number (FSN). The unit unification was completed using a conversion formula provided by the smoke meter



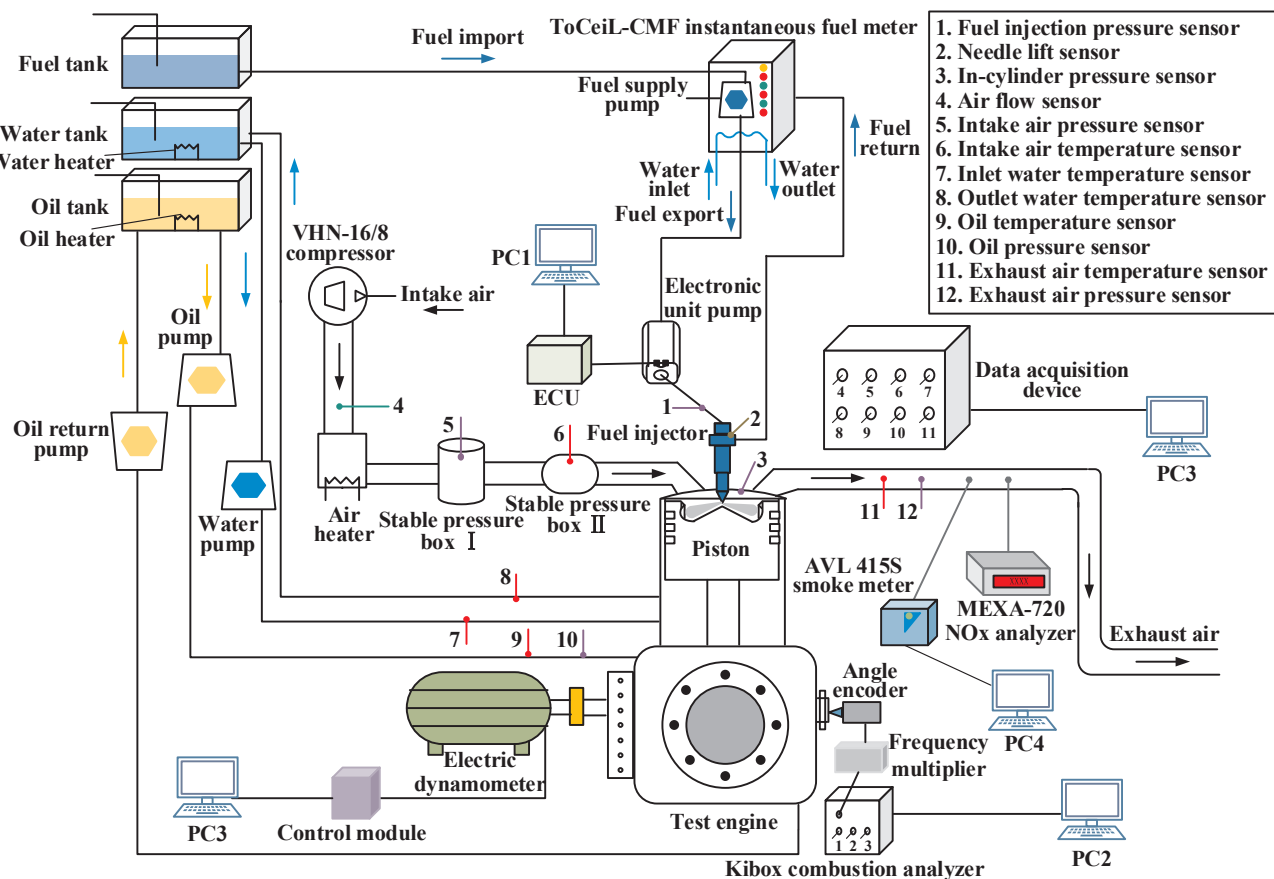


Fig. 7. Pedestal diagram of the engine.

specification. Fig. 6 shows the comparison of the experimental and computational results, and great consistency can be observed. Thus, the numerical models, the boundary conditions and the computational results of the simulation are credible.

2.3. Experimental setup

The test was conducted in a 132-mm single-cylinder diesel engine, the basic parameters of which have been listed in Table 1. The pedestal diagram of the engine is shown in Fig. 7.

To simulate the function of turbocharging, a VHN-16/8 air compressor was used to increase the intake air pressure, and a controllable heater was used to maintain a proper and constant intake air temperature. A straight intake port was designed in the cylinder head of the engine, and two intake and exhaust valves were adopted. An electronic unit pump created by Bosch was used for the fuel supply, in which the diameter and the pre-stroke of the plunger were 12 mm and 9 mm respectively. To measure the fuel consumption, a ToCeil-CMF instantaneous fuel meter equipped with fuel heating and thermostatic control was employed. The fuel meter has a response time of 0.1 s and an accuracy within 0.1% of the output.

An electric dynamometer was used to control the engine speed and measure the brake torque. The accuracies of the torque and speed are within $\pm 0.2\%$ FS and ± 2 r/min, respectively. The in-cylinder pressure was measured by a Kistler 6052 pressure sensor with an accuracy of $\pm 0.1\%$ FSO. The pedestal was equipped with a Kibox combustion analyzer to receive the in-cylinder measurement data and achieve the relevant combustion analysis.

An AVL 415S smoke meter was chosen to measure the soot level of

the exhaust gas with an accuracy of ± 0.2 FSN. A HORIBA MEXA-720 NOx analyzer was adopted to measure the NOx concentration. When the NOx concentration ranges from 0 to 1000 ppm, the accuracy is within ± 30 ppm. When the NOx concentration ranges from 1001 to 2000 ppm, the accuracy is within $\pm 3\%$ of the output.

To ensure a steady operating state, the temperatures of intake air, fuel supply, oil supply and outlet water were controlled within $60 \pm 2^\circ\text{C}$, $40 \pm 2^\circ\text{C}$, $70 \pm 5^\circ\text{C}$ and $80 \pm 5^\circ\text{C}$, respectively.

3. Results and discussion

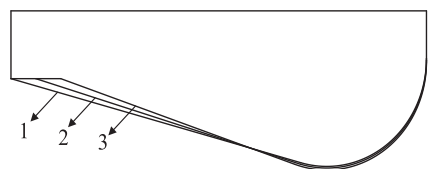
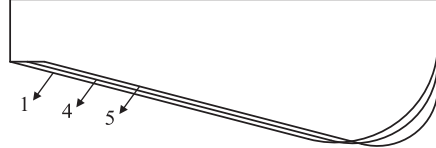
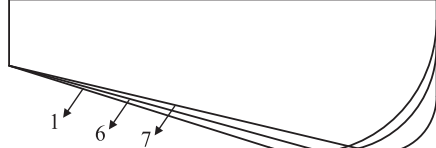
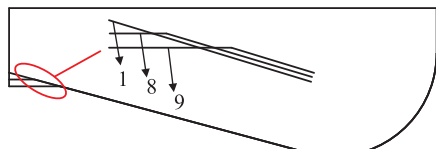
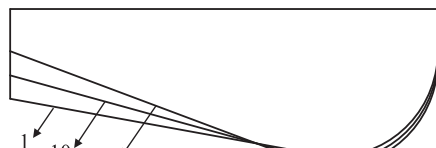
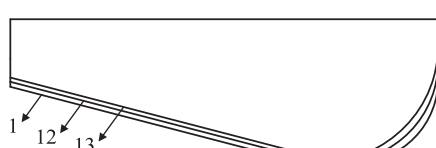
3.1. Effects of the central boss geometry on the performance of the LSCS

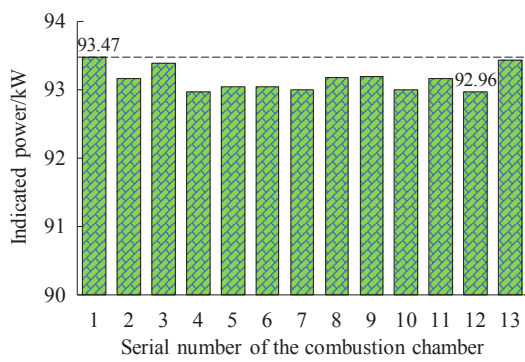
Based on the geometry of the reference chamber, twelve combustion chambers with different central boss geometries were modeled. A constant compression ratio of 13.5 was maintained, so the combustion chambers were created by changing two geometries simultaneously, as shown in Table 5, in which the No. 1 combustion chamber represented the reference chamber.

Fig. 8 shows the combustion performance (including the indicated power, soot and NOx emission) at various central boss geometries. It can be observed that the No. 1 combustion chamber performed the best. Its indicated power, soot emission, and NOx emission was 93.47 kW, 4.23 ppm, and 1566.4 ppm, respectively. In contrast, the indicated power was 92.96 kW and the soot emission was higher in the No. 12 combustion chamber. But on the whole, the indicated power showed slight differences at various central boss geometries, and the amplitude of variation was only 0.51 kW. Considering the design principle of the LSCS, the jet spray interacts primarily with the split-flow creation

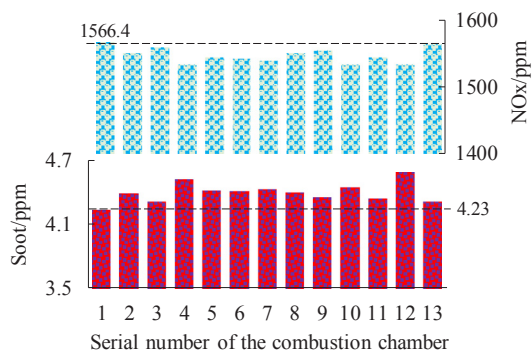
Table 5

Combustion chambers with different central boss geometries.

| Serial number | Variable geometries | r_t/mm | $\delta_t/^\circ$ | h_t/mm | r_c/mm | Sketch maps |
|---------------|---------------------|-----------------|-------------------|-----------------|-----------------|---|
| 1 | $r_t - \delta_t$ | 0 | 15 | 7.5 | 12 |  |
| 2 | | 3 | 16.6 | 7.5 | 12 | |
| 3 | | 6 | 18.7 | 7.5 | 12 | |
| 1 | $r_t - r_c$ | 0 | 15 | 7.5 | 12 |  |
| 4 | | 2 | 15 | 7.5 | 9.9 | |
| 5 | | 4 | 15 | 7.5 | 7.1 | |
| 1 | $\delta_t - r_c$ | 0 | 15 | 7.5 | 12 |  |
| 6 | | 0 | 13 | 7.5 | 6.3 | |
| 7 | | 0 | 17 | 7.5 | 15.2 | |
| 1 | $r_t - h_t$ | 0 | 15 | 7.54 | 12 |  |
| 8 | | 3 | 15 | 8.34 | 12 | |
| 9 | | 6 | 15 | 9.13 | 12 | |
| 1 | $\delta_t - h_t$ | 0 | 15 | 7.5 | 12 |  |
| 10 | | 0 | 10 | 10.2 | 12 | |
| 11 | | 0 | 20 | 4.8 | 12 | |
| 1 | $h_t - r_c$ | 0 | 15 | 7.5 | 12 |  |
| 12 | | 0 | 15 | 7.0 | 10 | |
| 13 | | 0 | 15 | 8.2 | 14 | |



(a) Indicated power



(b) Soot and NOx emission

Fig. 8. Combustion performance at various central boss geometries.

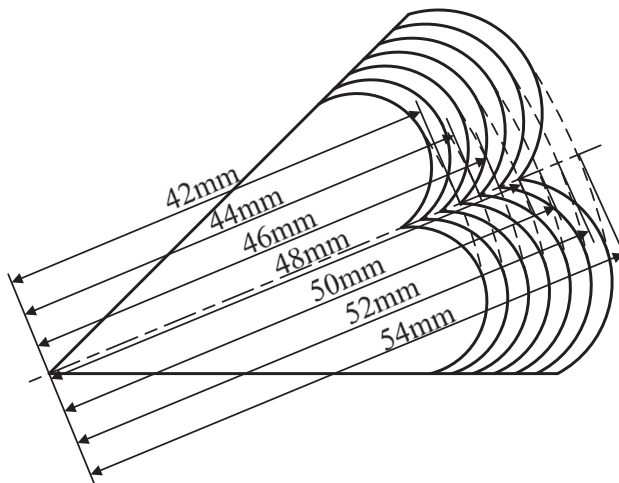


Fig. 9. Sketch maps of the split-flow creation at various combustion chamber diameters.

rather than the central boss. Therefore, it has been found that the central boss geometry has little effect on the combustion performance of the LSCS.

3.2. Effects of the split-flow creation geometry on the combustion performance of the LSCS

The geometrical match of the split-flow creation is closely linked to fuel supply systems. Spray characteristics are quite different at various nozzle hole diameters and fuel injection pressures; therefore, suitable split-flow creation should be designed to match with the specific fuel supply system. In this study, the numerical setup of the fuel injection parameters was done in accordance with the fuel supply system of the test engine. Hence, the relevant conclusions are based on the tested fuel supply system.

Considering the geometrical relationship of D , h_a , and r_a , as Eq. (1) shown, only the effects of D and h_a on the LSCS combustion performance were studied. Then, a series of combustion chambers with different D and h_a were modeled. For a constant compression ratio, h_t was taken as the adjustable parameter because of its slight effect on combustion performance.

3.2.1. Effects of the combustion chamber diameter

Fig. 9 shows the sketch maps of the split-flow creation at various combustion chamber diameters ranging from 84 to 108 mm (the combustion chamber radius ranged from 42 to 54 mm). The other combustion chamber geometries were consistent with the reference chamber, except for the adjustable parameter h_t . The combustion chamber depth varied greatly with the combustion chamber diameters such that the corresponding optimal spray angle also varied greatly. Therefore, a suitable spray angle was matched with each combustion chamber before studying the effect of the combustion chamber diameter.

Fig. 10 shows the matching results of the spray angle at various combustion chamber diameters. When D was 84 and 88 mm, the LSCS with a spray angle of 145° obtained the lowest soot emission and the highest indicated power, exerting the best combustion performance. Moreover, it can be observed that the NOx emission and soot emission was negatively correlated, which conformed to the recognized trade-off relation of soot and NOx. However, when the value of D was in a larger range of 92–104 mm, the optimal spray angle of the LSCS was 150°; when D increased to 108 mm, the matching result of the spray angle

turned into 155°. Obviously, the matching spray angle of the LSCS increases with an increase in combustion chamber diameter due to the augment of the combustion chamber depth, as shown in Fig. 10(h).

After matching spray angles, the effects of the combustion chamber diameter were analyzed by comparing the combustion performance of the LSCS at various combustion chamber diameters, and Fig. 11 shows the comparative results. Evidently, when D was 92 mm, the LSCS obtained the best combustion performance, rendering the lowest soot emission and the highest indicated power; meanwhile, the highest NOx emission was observed because the in-cylinder high-temperature environment is in favor of the NOx formation. Regardless of whether D decreased or increased from 92 mm, the combustion performance uniformly deteriorated; especially when D was less than 88 mm or more than 104 mm, the deterioration was intense. Therefore, an optimal value of D should be chosen to benefit the combustion performance of the LSCS.

To reveal the influence mechanism of the combustion chamber diameter on the LSCS combustion performance, the numerical results of the in-cylinder fuel/air equivalence ratio were compared, as shown in Fig. 12. Another study [27] concluded that interference of neighboring fuel spray jets benefits the fuel/air mixing of the LSCS; therefore, the in-cylinder fuel/air equivalence ratio of the neighboring fuel spray jets was also compared. When D was 92 mm, the jet spray split into two lateral swirls after colliding with the convex edge, promoting the fuel diffusion, as shown in Fig. 12(a). After flowing out from the split arcs, the neighboring lateral swirls converged and intervened at an angle of 38.8°, and the fuel/air mixture formation in the interferential fuel zone was improved, as shown in Fig. 12(b). When D was 84 mm, the wall impingement appeared earlier and more fuel flowed into the interferential fuel zone at an angle of 28°. In this case, the decreasing interferential angle weakened the effectiveness of the interference; meanwhile, the circumferential available air in the interferential fuel zone decreased due to the diminution of the combustion chamber diameter. Therefore, it can be observed that a large mass of concentrated fuel/air mixture accumulated in the interferential fuel zone after the end of the fuel injection.

However, conditions were entirely different at large values of D . When D was 100 mm, the distance between the nozzle hole and the split-flow creation increased. After a fuel jet spray collided with the convex edge, the development and diffusion of the lateral swirls were not sufficient because of the lessened spray energy and the deflected impingement direction. The poor development and diffusion of the lateral swirls were more conspicuous at a D of 108 mm because plentiful concentrated fuel/air mixture accumulated in the split arcs after the end of the fuel injection. In short, an inappropriate D worsens the LSCS combustion performance due to the accumulation of concentrated fuel/air mixture in the interferential fuel zone or split arcs. As a result, it has been found that D has a significant effect on the diffusion of the fuel spray and the formation of the fuel/air mixture.

3.2.2. Effects of the convex edge height

The aforementioned results indicate that the development and diffusion of the lateral swirls were not sufficient in the reference combustion chamber ($D = 100$ mm). For the sake of studying the effects of the convex edge height precisely, in addition to the reference combustion chamber, another auxiliary reference combustion chamber with a diameter of 92 mm was analyzed, the central boss geometries of which were the same as the reference combustion chamber, except for the adjustable parameter h_t . According to the geometrical calculation, when D is 92 mm and 100 mm, the possible values of h_a are in the range of 0–8.25 mm and 0–8.96 mm, respectively; therefore, two groups of combustion chambers (D92 and D100) were modeled, in which h_a

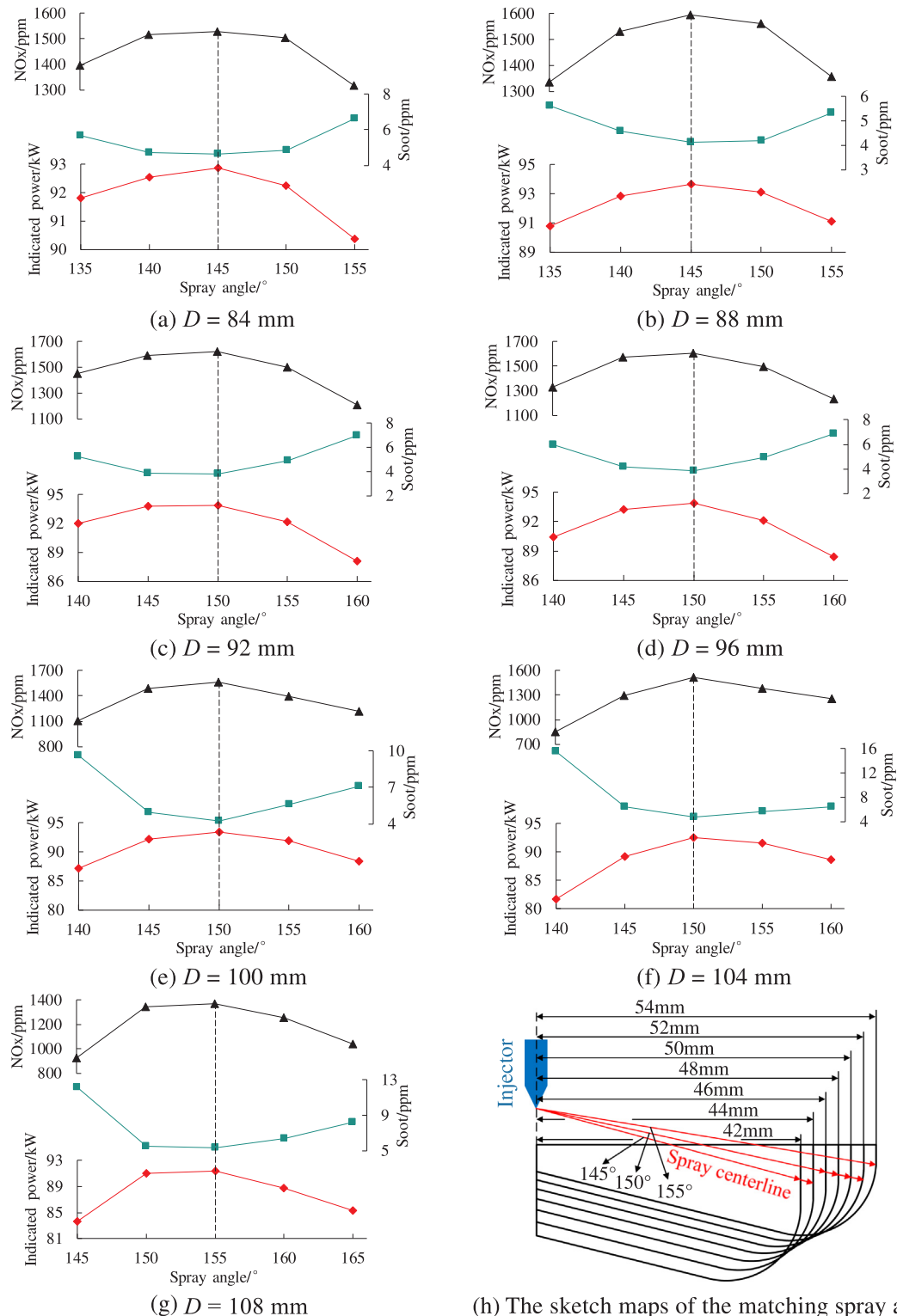


Fig. 10. Matching results of the spray angle at various combustion chamber diameters.

ranged from 0 to 8.2 mm and 0 to 8.9 mm, respectively. Fig. 13 shows the sketch maps of the split-flow creation at various convex edge heights.

Fig. 14 shows the combustion performance of the LSCS at various convex edge heights, in which all combustion chambers matched

optimal spray angles. For the D92 chambers, when h_a was 6 mm, the LSCS obtained the highest indicated power and the lowest soot emission, revealing the best combustion performance; when h_a decreased or increased from 6 mm, the combustion performance deteriorated, and the deterioration became more serious in cases when h_a was close to the

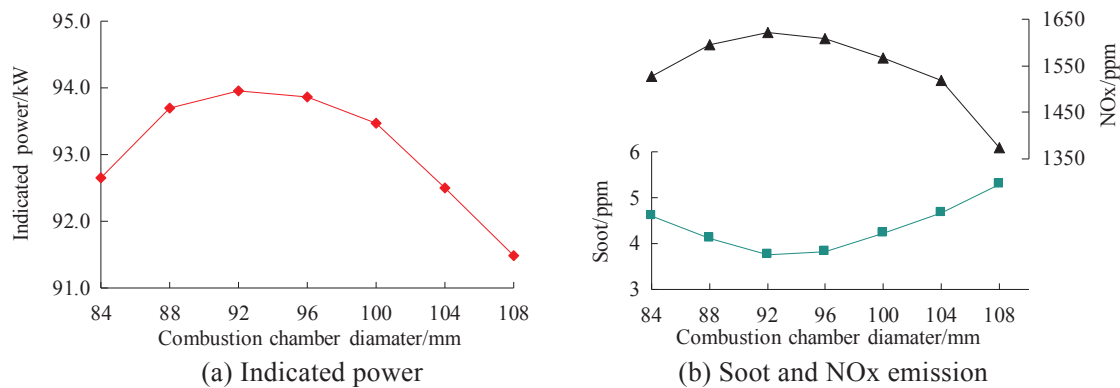


Fig. 11. Combustion performance at various combustion chamber diameters.

maximum and minimum limits; moreover, the LSCS showed the worst combustion performance at the maximum convex edge height. For the D100 chamber, these tendencies were also observed, except that the optimal value of h_a changed into 7 mm. Therefore, to benefit the combustion performance of the LSCS, a proper value of h_a should be chosen based on the combustion chamber diameter.

To reveal the influence mechanism of the convex edge height on the LSCS combustion performance, the in-cylinder fuel/air equivalence ratio in the D92 chambers was analyzed, as shown in Fig. 15. When h_a was 6 mm, the formation of the lateral swirls promoted the fuel diffusion; meanwhile, the interference at an angle of 38.8° improved the fuel/air mixture formation in the interferential fuel zone. When h_a was 8.2 mm, the jet spray collided with the convex edge earlier, and the direction of the spray centerline was almost coinciding with the tangent of the split arc. Therefore, a large mass of fuel gathered in the interferential fuel zone at a small angle of 0.8°, causing an accumulation of the concentrated fuel/air mixture because of the negligible interference of the neighboring fuel spray jets, as shown in Fig. 15(b). Therefore, the combustion performance of the LSCS was significantly worsened. However, conditions were entirely different at small values of h_a (similar to the cases of large combustion chamber diameters discussed in 3.2.1). When h_a was 4 mm, the nozzle hole was far away from the split-flow creation, and the jet spray collided with the convex edge at a large angle of 40.5°. The lessened spray energy and increased energy loss of impingement restricted the development and diffusion of the lateral swirls. The restriction was more conspicuous at a smaller h_a of 2 mm, with the result that a large mass of concentrated fuel/air mixture accumulated in the split arcs after the end of the fuel injection. Therefore, an unsuitable h_a causes the accumulation of concentrated fuel/air mixture in the interferential fuel zone or split arcs, impairing the combustion performance of the LSCS.

3.3. Optimization of the LSCS chamber geometry

Before optimizing the LSCS chamber geometry, a sensitivity analysis on the indicated power was conducted to confirm the influence levels of the geometries on the LSCS combustion performance. A concept of sensitivity Φ [28] was adopted to represent the sensitivities on the indicated power at various geometries, as follows:

$$\Phi_x^{P_i} = \left| \frac{\Delta P_i / P_i}{\Delta x / x} \right| = \left| \frac{\partial P_i / \partial x}{P_i / x} \right| \quad (3)$$

$\Phi_x^{P_i}$ is a dimensionless parameter that reflected the relative varying gradient of the indicated power with the variation of the geometries. The values of $\partial P_i / \partial x$ at minimum and maximum boundaries are equal to

the right and left slopes, respectively, while the other values averaged across both slopes. Then, sensitivities at various central boss geometries were calculated aiming at six parameter combinations (including $r_t - \delta_b$, $r_t - r_c$, $\delta_t - r_c$, $r_t - h_b$, $\delta_t - h_t$ and $h_t - r_c$); for the split-flow creation geometry, the sensitivities of D and h_a were analyzed.

Fig. 16 shows the sensitivities of the LSCS geometries on the indicated power. The rectangles represent the average sensitivities, and the upright lines represent the sensitivity ranges. It can be observed that the sensitivity ranges and the mean values of split-flow creation geometries are large, while those of the central boss geometries are small and even negligible, except for the combination of h_t and r_c . Moreover, the sensitivity range and the average of D is much larger than the other geometries. Obviously, the split-flow creation rather than the central boss primarily affects the combustion performance of LSCS. Therefore, D and h_a were regarded as the main objects for geometrical optimization. Then, a suitable combination of h_t and r_c was matched.

Based on the reference combustion chamber, five groups of combustion chambers were simulated, the diameters of which were 84, 88, 92, 96 and 100 mm, respectively. Each group contained five combustion chambers with different convex edge heights. Then, the combustion performance at various split-flow creation geometries was compared, as shown in Fig. 17. The left side shows the three-dimensional surface charts, and the right side shows the contour maps. It can be observed that the optimal convex edge heights ($h_{a,\text{opt}}$) were different at various combustion chamber diameters. As D increased from 84 to 100 mm, the corresponding $h_{a,\text{opt}}$ varied from 5 to 7 mm. This is because when the value of D is small, the convex edges closed to the nozzle holes and the energy of the spray impingement was sufficient. In this case, split-flow creations with a relatively small value of h_a promoted the development of the lateral swirls in the split arcs and the mixing of fuel and air in the interferential fuel zone; however, a larger h_a caused the accumulation of concentrated fuel/air mixture in the interferential fuel zone. Additionally, the data in Fig. 17 indicates that, when D was 88, 92 and 96 mm, and the corresponding value of h_a was optimal, the LSCS showed excellent and approximate combustion performance. This reveals that the key to designing an efficient split-flow creation is finding a reasonable match between D and h_a rather than focusing on a single value of either. When D was 92 mm and h_a was 6 mm, the LSCS obtained the best indicated power of 93.90 kW and the lowest soot emission of 3.76 ppm. Therefore, the optimal results of the split-flow creation geometries are as follows: $D = 92$ mm, $h_a = 6$ mm.

Based on the optimal results of split-flow creation geometries, combustion chambers with different connective arc radii (r_c) were modeled and simulated. To maintain a constant compression ratio, the values of h_t were adjusted at various connective arc radii, as shown in Fig. 18.

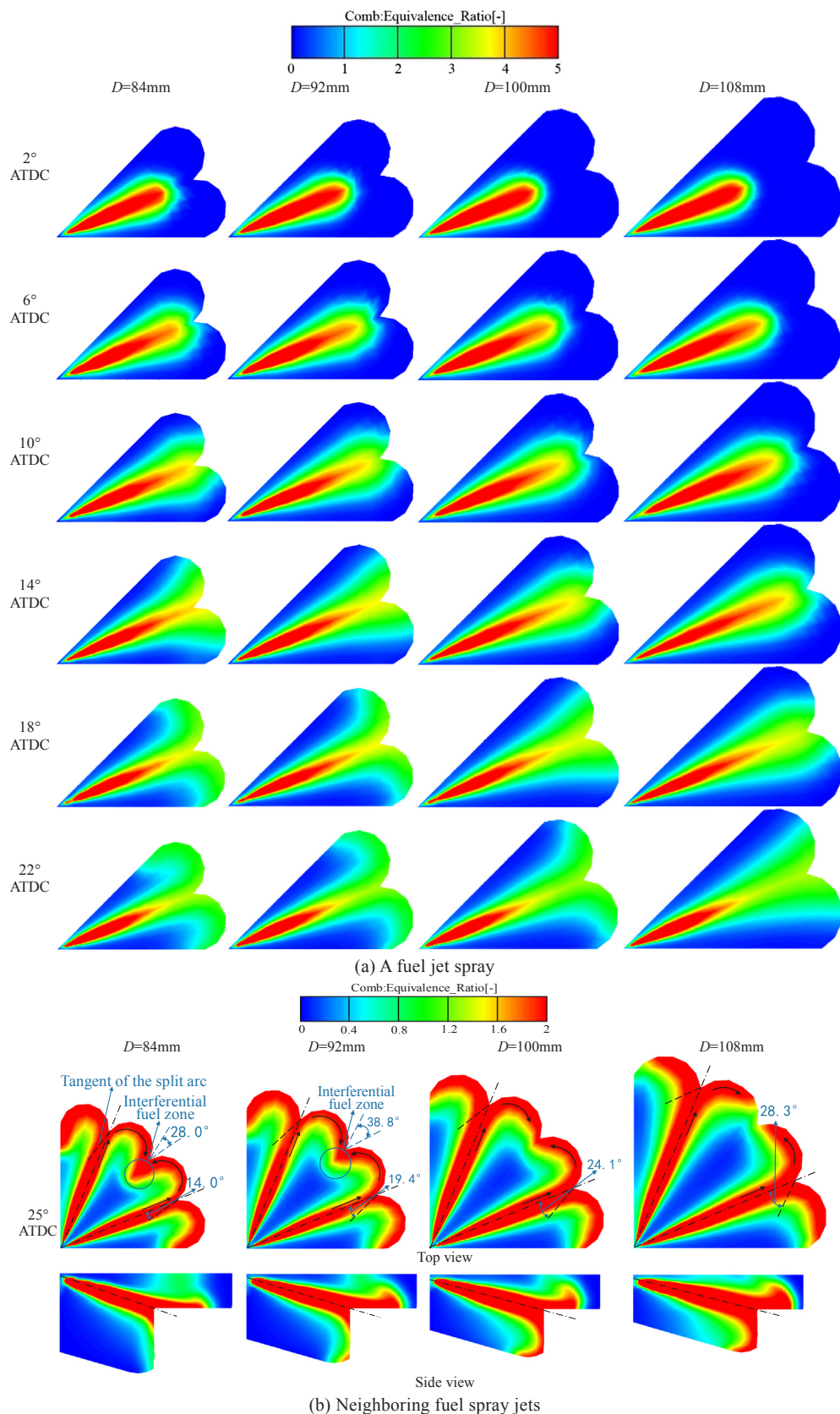


Fig. 12. In-cylinder fuel/air equivalence ratio at various combustion chamber diameters.

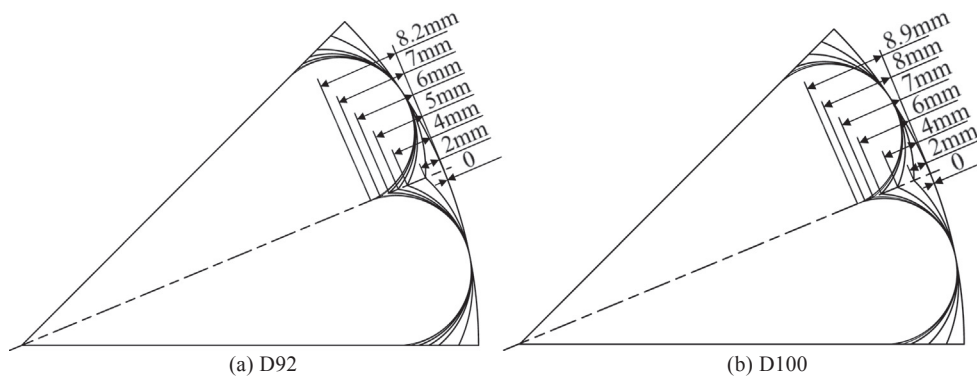


Fig. 13. Sketch maps of the split-flow creation at various convex edge heights.

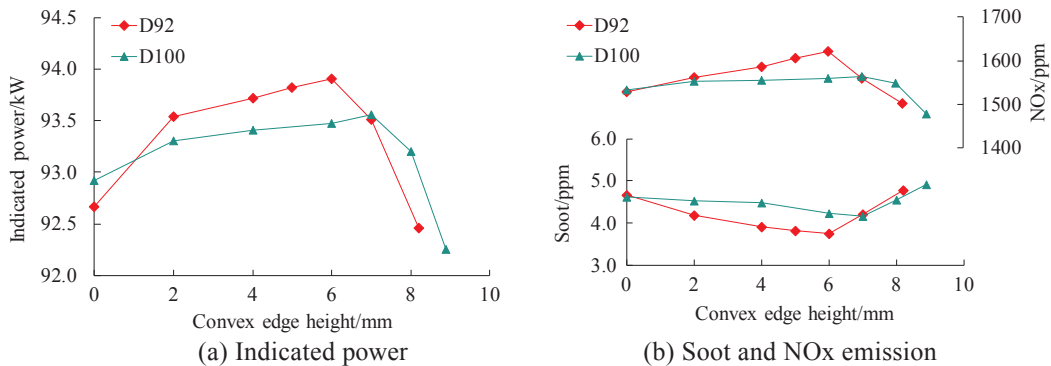


Fig. 14. Combustion performance at various convex edge heights.

Fig. 19 shows the combustion performance at various connective arc radii. When r_c was less than 12 mm, a slight distinction was detected in the indicated power as well as with the soot and NOx emission. In these cases, the variation of r_c primarily affected the structure of the bottom combustion chamber, where the formation and combustion of fuel/air mixture rarely occurred. However, when r_c increased from 12 mm, the combustion performance deteriorated significantly. This is because in cases of a large r_c , the tangency point between the connective arc and the lateral wall surface was close to the top of the combustion chamber, so the shrinkage of the space near the split-flow creation weakened the wall-flow-guided effectiveness. As such, when r_c was 12 mm, the LSCS obtained the best indicated power and the lowest soot emission. Therefore, the optimal results of r_c and h_t are 12 mm and 11.1 mm, respectively.

Based on the discussion above, the optimal LSCS chamber geometries are listed in Table 6.

3.4. Performance verification of the optimized LSCS

Based on the optimal LSCS chamber geometries, a new piston was processed and applied to the test engine. Fig. 20 shows the geometry and photograph of the test piston.

The double swirl combustion system (DSCS), proposed by our laboratory, is another kind of WFGCS [29]. In the DSCS, a circular ridge is created to divide a combustion chamber into an inner chamber and an outer chamber, as shown in Fig. 21. After a fuel jet spray impinges the circular ridge, two swirls form in the inner and outer chamber respectively so that the fuel/air mixture formation is improved [30]. So far, the DSCS has been studied for several decades, and its excellent fuel

economy and soot emission have been successfully attested [31]. As a result, the DSCS was set as a comparison to verify and evaluate the combustion performance of the LSCS.

In the verification test, the engine speeds were set at 1300, 1500, 1800 and 2100 r/min, and the corresponding brake power was set at 27, 36, 43 and 52 kW, respectively. Under each experimental condition, the fuel consumption was determined by averaging 5 measurements, and the soot and NOx emission was acquired by averaging 3 measurements. The errors of the fuel consumption and soot emission are within 0.1% of the output and 0.2 FSN, respectively. In the ranges of 0–1000 ppm and 1001–2000 ppm, the errors of the NOx emission are within ± 30 ppm and $\pm 3\%$ of the output, respectively. Fig. 22 shows the combustion performance of the LSCS and DSCS at various engine speeds. It can be observed that the combustion performance of the optimized LSCS improved conspicuously on the basis of the original LSCS, especially the soot emission. Compared with the DSCS, the fuel consumption of the optimized LSCS decreased by 2.8–4.1 g/(kW·h) at various engine speeds. Therefore, the optimized LSCS shows excellent combustion performance and application potential in terms of fuel economy. Moreover, the soot emission also showed a significant reduction—in the range of 69–75%. Obviously, the optimized LSCS has significant positive effects on reducing soot emission due to the successful functions of the diffusion of fuel, the formation of fuel/air mixture and the improvement of local concentrated fuel/air mixture. During the combustion process, the proper temperatures and oxygen concentration environments caused increasing NOx emission, which could be solved effectively by an appropriate Selective Catalytic Reduction (SCR) system.

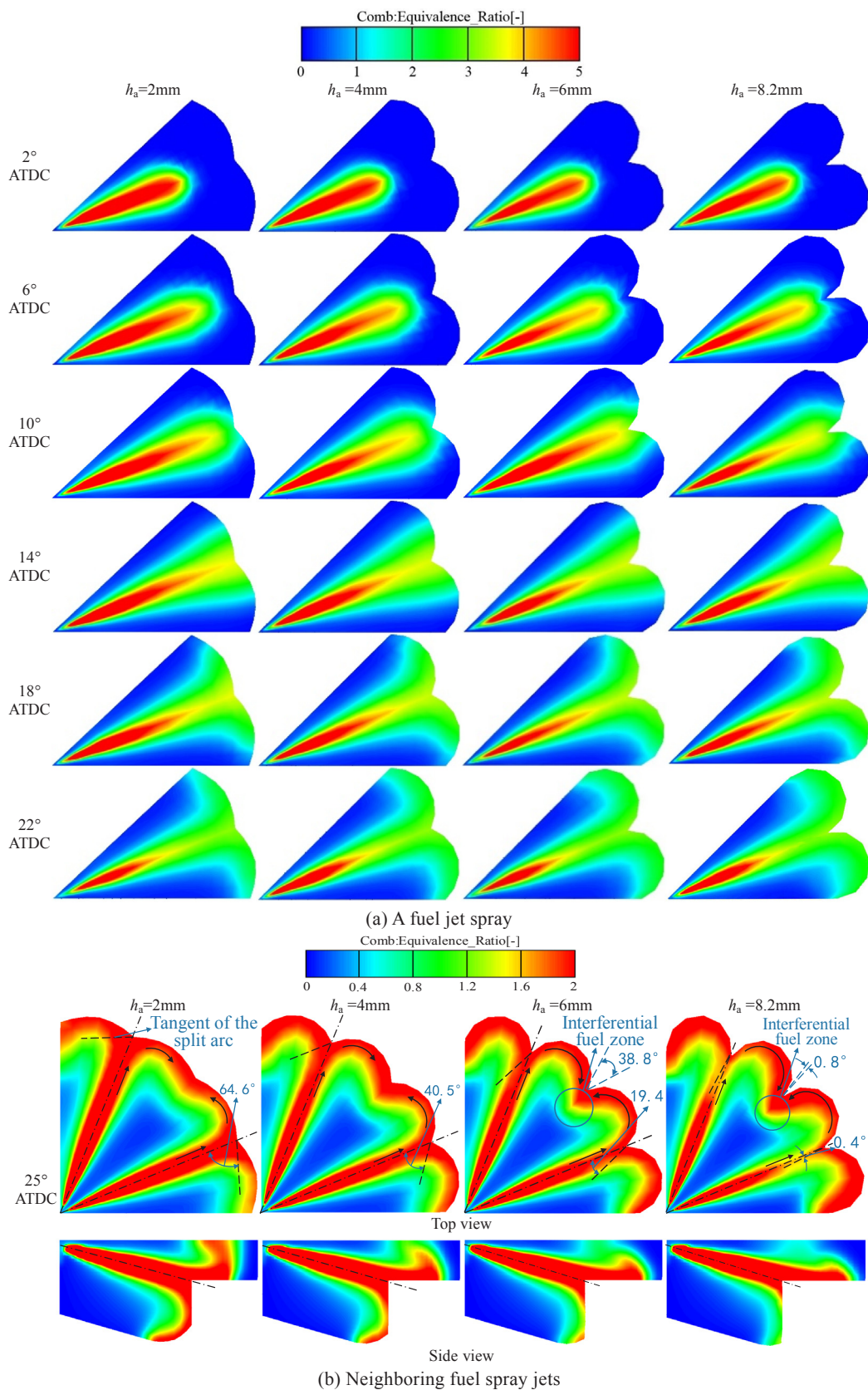


Fig. 15. In-cylinder fuel/air equivalence ratio at various convex edge heights.

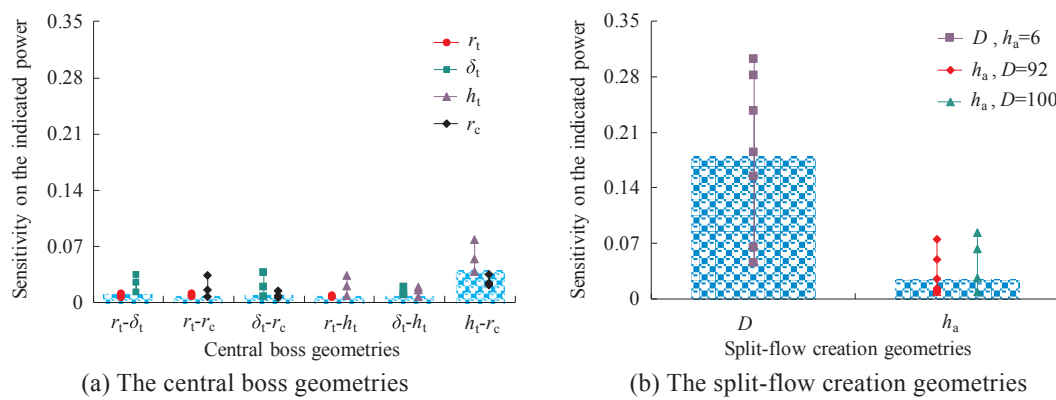


Fig. 16. Sensitivities of the LSCS geometries on the indicated power.

3.5. Matching method of the LSCS chamber geometry

In the LSCS, the split-flow creation rather than the central boss primarily affects the combustion performance. As such, when the values of r_t , δ_t , and r_c were 0, 15° and 12 mm, respectively, the LSCS with the same split-flow creation geometry showed better combustion performance. As a result, r_t , δ_t and r_c can be considered as constant parameters in the geometrical match of the LSCS chamber, while h_t was taken as the adjustable parameter to ensure constant compression ratio.

Numerical results indicate that the influence mechanisms of D and h_a on the combustion performance are similar. In fact, varying split-flow creation geometries resulted in different integrated effects of the lateral swirls diffusion in the split arcs and the fuel/air mixture formation in the interferential fuel zone. Importantly, the angle between the spray centerline and the tangent of the corresponding split arc significantly impacted the integrated effectiveness. To analyze the relation between the angle and split-flow creation geometry, the angle was defined as the deviation angle of flow-guide θ , as shown in Fig. 23. The value of θ can be calculated as follows:

$$\theta = \arccos \left\{ \left[\frac{D^2 \left(1 - \cos \frac{\beta}{4}\right) + 2Dh_a \cos \frac{\beta}{4}}{D \left(1 - \cos \frac{\beta}{4}\right) (D - 2h_a) + 2h_a^2} - 1 \right] \sin \frac{\beta}{4} \right\}, \quad \theta \in \left[0, \frac{\pi}{2} \right] \quad (4)$$

Tables 7 and 8 list the deviation angles at various combustion chamber diameters and convex edge heights, respectively. It can be observed that θ increased with an increasing D and decreasing h_a . The results discussed in 3.2 indicate that accumulation of the concentrated fuel/air mixture in the split arcs appeared when the value of θ was too large; conversely, the concentrated fuel/air mixture accumulated in the interferential fuel zone. Therefore, a suitable value of θ should be chosen for better combustion performance of the LSCS.

When the optimal convex edge height was matched with the combustion chamber diameter, the split-flow creation geometry was considered suitable. Fig. 17 shows that as D increased from 84 to 100 mm, the corresponding $h_{a,\text{opt}}$ varied from 5 to 7 mm. Table 9 lists the deviation angles of flow-guide on condition of suitable split-flow creation geometry. The data indicates that the values of θ were in a specific range of 15–27°. Therefore, when the LSCS is applied to different fuel supply systems, the range can provide an important reference for the geometrical match of the split-flow creation.

From the above, to match the LSCS chamber geometry with diverse fuel supply systems, a representative method can be summarized. The values of r_t , δ_t and r_c can be set at 0, 15° and 12 mm, respectively, while h_t is the adjustable parameter to maintain a constant compression ratio.

The value of θ can be set in the range of 15–27°. Therefore, only the value of D needs to be matched, and h_a can be determined afterward. Then, the geometrical match of the LSCS chamber with the specific fuel supply system is complete.

4. Conclusions

The effects of the LSCS chamber geometries on the combustion and emission characteristics of DI diesel engines were studied using numerical simulation under the condition of 2500 r/min and full load. Then, based on a sensitivity analysis on the indicated power, the LSCS geometry was optimized. The optimized LSCS showed excellent combustion performance in the test engine. To efficiently apply the LSCS in different fuel supply systems, a representative matching method of LSCS chamber geometry was proposed based on the relevant findings. The main conclusions are summarized below:

- (1) In the LSCS geometry, the split-flow creation geometry primarily affects combustion performance, in which θ (the deviation angle of flow-guide) plays a dominant role. When θ is in the range of 15–27°, the LSCS obtains better wall-flow-guided effectiveness and combustion performance. Too large values of θ cause the accumulation of concentrated fuel/air mixture in the split arcs, while too small values of θ cause the concentrated fuel/air mixture accumulate in the interferential fuel zone.
- (2) The optimized LSCS shows better combustion performance compared with the DSCS, especially in terms of fuel consumption and soot emission. To be specific, the fuel consumption decreased by 2.8–4.1 g/(kW·h) and the soot emission decreased in the range of 69–75% at various engine speeds ranging from 1300 to 2100 r/min.
- (3) Aiming at diverse fuel supply systems, the LSCS chamber geometry can be conveniently matched in the following method:

The values of r_t (the central boss radius), δ_t (the inclination angle of the central boss) and r_c (the connective arc radius) can be set as 0, 15° and 12 mm, respectively, while h_t (the central boss depth) is the adjustable parameter to maintain a constant compression ratio. The value of θ can be set in the range of 15–27°. Therefore, only the value of D (the combustion chamber diameter) needs to be matched with the specific fuel supply system, and then the LSCS chamber geometry can be determined.

In this method, the match of D is related to the specific fuel supply system; however, the match of θ is universal.

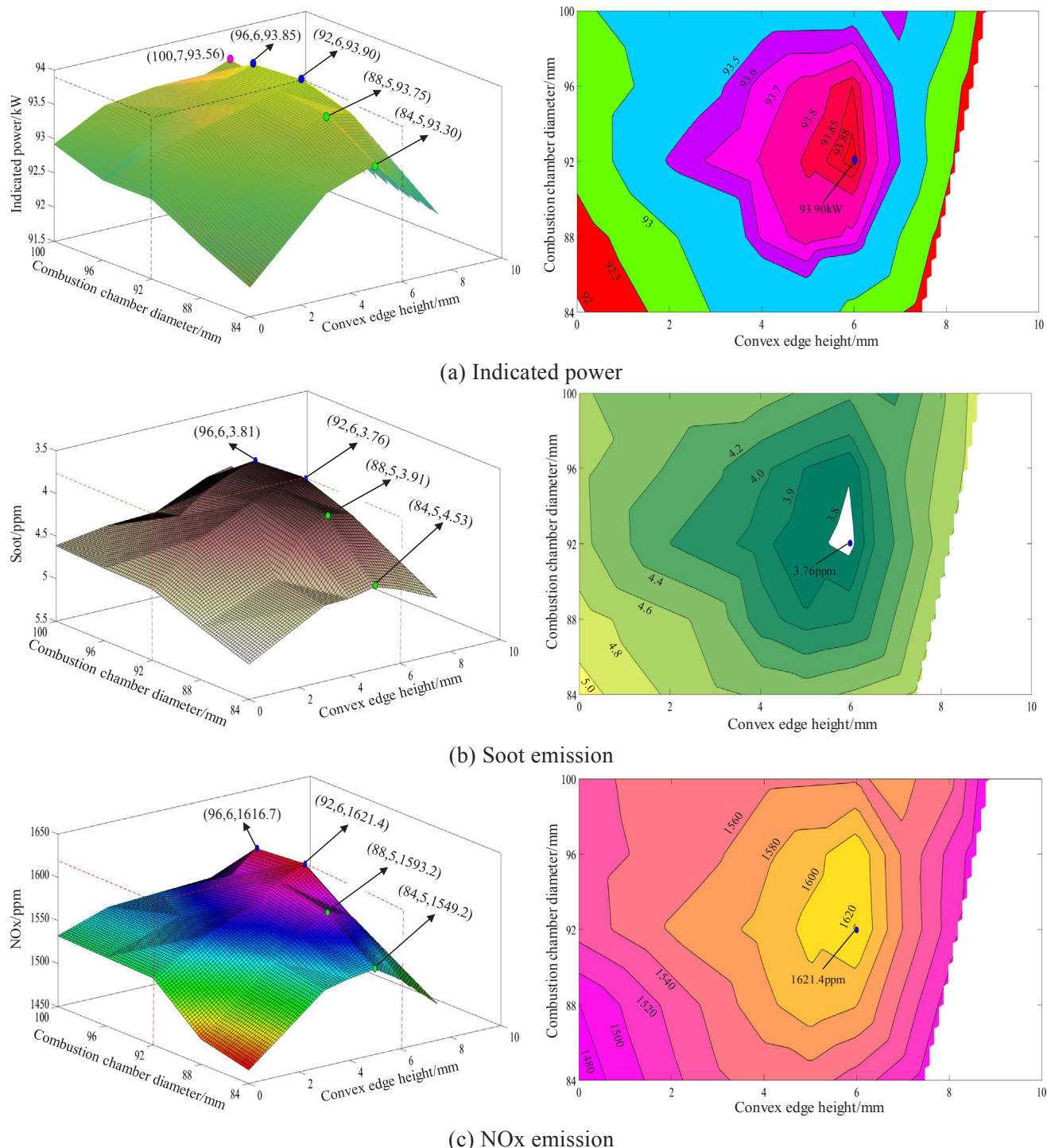


Fig. 17. Combustion performance at various split-flow creation geometries.

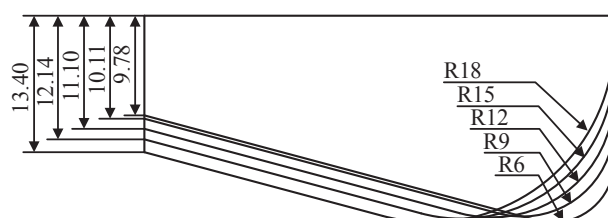


Fig. 18. Sketch maps of the split-flow creation at various connective arc radii.

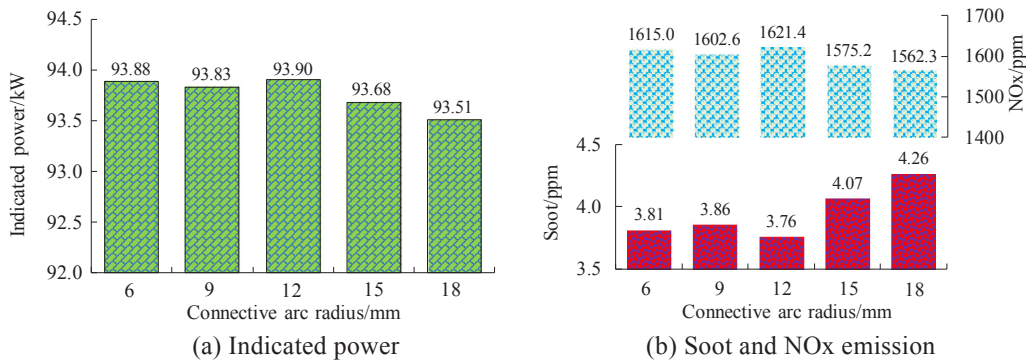


Fig. 19. Combustion performance at various connective arc radii.

Table 6
Optimal LSCS chamber geometries.

| | | |
|--------------------------------|--|------|
| Central boss geometries | Central boss radius r_t (mm) | 0 |
| | Inclination angle of central boss δ_t (°) | 15 |
| | Central boss depth h_t (mm) | 11.1 |
| | Connective arc radius r_c (mm) | 12 |
| Split-flow creation geometries | Combustion chamber diameter D (mm) | 92 |
| | Convex edge height h_a (mm) | 6 |

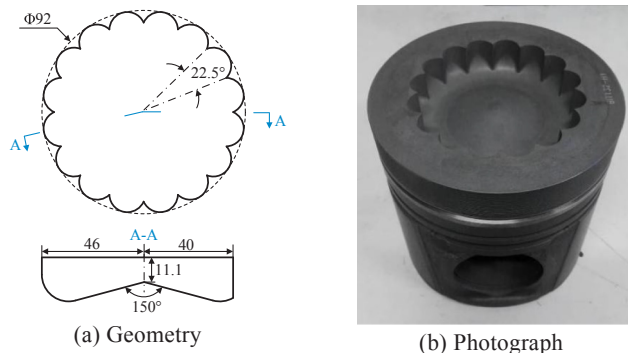


Fig. 20. Geometry and photograph of the test piston.

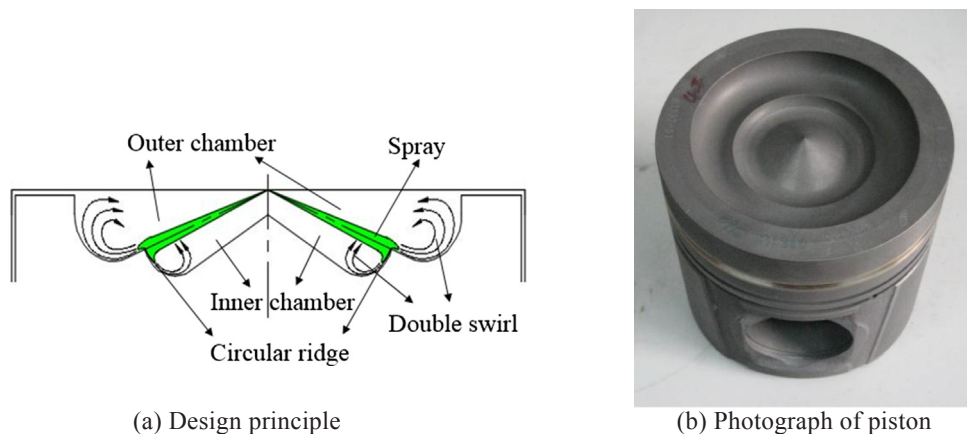
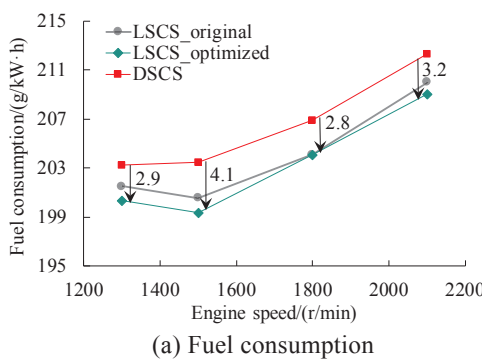


Fig. 21. Design principle and piston of the DSCS.



(a) Fuel consumption

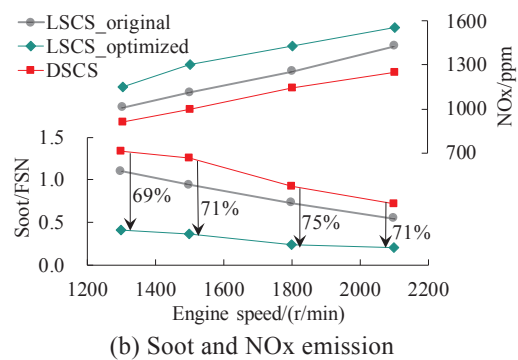


Fig. 22. Combustion performance of the LSCS and DSCS at various engine speeds.

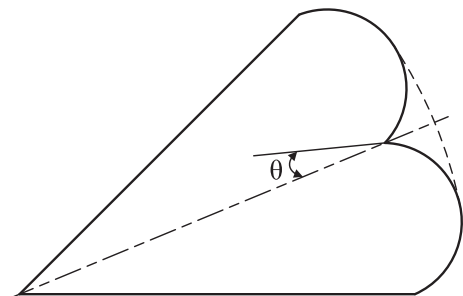


Fig. 23. Deviation angle of flow-guide.

Table 7
Deviation angles of flow-guide at various combustion chamber diameters.

| D/mm | 84 | 88 | 92 | 96 | 100 | 104 | 108 |
|-----------------|------|------|------|------|------|------|------|
| $\theta/^\circ$ | 14.0 | 16.8 | 19.4 | 21.8 | 24.1 | 26.3 | 28.3 |

Table 8
Deviation angles of flow-guide at various convex edge heights.

| D92 | h_a/mm | Deviation angles of flow-guide at various convex edge heights | | | | | | |
|------|-----------------|---|------|------|------|------|------|-----|
| | | 0 | 2 | 4 | 5 | 6 | 7 | 8.2 |
| D100 | h_a/mm | 90 | 64.6 | 40.5 | 29.5 | 19.4 | 10.2 | 0.4 |
| | | 0 | 66.6 | 44.1 | 24.1 | 15.2 | 7.1 | 0.5 |

Table 9
Deviation angles of flow-guide on condition of suitable split-flow creation geometry.

| $D/\text{mm}(h_{a,\text{opt}}/\text{mm})$ | 84(5) | 88(5) | 92(6) | 96(6) | 100(7) |
|---|-------|-------|-------|-------|--------|
| $\theta/^\circ$ | 24.6 | 27.1 | 19.4 | 21.8 | 15.2 |

References

- [1] Li X, Qiao Z, Su L, Li X, Liu F. The combustion and emission characteristics of a multi-swirl combustion system in a DI diesel engine. *Appl Therm Eng* 2017;115:1203–12.
- [2] Jafarmadar S, Mansouri M. Exergy analysis of air injection at various loads in a natural aspirated direct injection diesel engine using multidimensional model. *Fuel* 2015;154:123–31.
- [3] Rakopoulos CD, Kosmadakis GM, Pariotis EG. Investigation of piston bowl geometry and speed effects in a motored HSDI diesel engine using a CFD against a quasi-dimensional model. *Energy Convers Manage* 2010;51(3):470–84.
- [4] Benajes J, Novella R, Pastor JM, Hernández-López A, Kokjohn SL. Computational optimization of the combustion system of a heavy duty direct injection diesel engine operating with dimethyl-ether. *Fuel* 2018;218:127–39.
- [5] Luo M, Xiang L, Li X. Numerical simulation of the effects of combustion chamber
- [6] Jaichandar S, Annamalai K. Combined impact of injection pressure and combustion chamber geometry on the performance of a biodiesel fueled diesel engine. *Energy* 2013;55:330–9.
- [7] Yong S, Fu-Shui L, Xiang-Rong L. Forced swirl combustion chamber in diesel engine: Numerical simulation and experimental research. *Environ Eng Manage J* 2011;2(7):34–7.
- [8] Yao M, Zheng Z, Liu H. Progress and recent trends in homogeneous charge compression ignition (HCCI) engines. *Prog Energy Combust Sci* 2009;35(5):398–437.
- [9] Qiao XQ, Song YC, Gao XY, Chen JH, Zhen H. Experimental study on umbrella-curtain spray combustion system for diesel engine. *J Shanghai Jiaotong Univ* 2004;38(7):1193–6.
- [10] Wei S, Wang F, Leng X, Liu X, Ji K. Numerical analysis on the effect of swirl ratios on swirl chamber combustion system of DI diesel engines. *Energy Convers Manage* 2013;75:184–90.
- [11] Zama Y, Odawara Y, Furuhata T. Experimental investigation on velocity inside a diesel spray after impingement on a wall. *Fuel* 2017;203:757–63.
- [12] Si Z, Shimasaki N, Nishida K, Ogata Y, Guo M, Tang C, et al. Experimental study on impingement spray and near-field spray characteristics under high-pressure cross-flow conditions. *Fuel* 2018;218:12–22.
- [13] Yu H, Liang X, Shu G, Wang Y, Zhang H. Experimental investigation on spray-wall impingement characteristics of n-butanol/diesel blended fuels. *Fuel* 2016;182:248–58.
- [14] Wang Z, Guo H, Wang C, Xu H, Li Y. Microscopic level study on the spray impingement process and characteristics. *Appl Energy* 2017;197:114–23.
- [15] Li X, Zhao W, Su L, Yang W, Qiao Z, Liu F. Combustion and emissions of a lateral-swirl combustion system in diesel engines. *Trans Csice* 2017;35(4):297–304.
- [16] Su L, Li X, Zhang Z, Liu F. Numerical analysis on the combustion and emission characteristics of forced swirl combustion system for DI diesel engines. *Energy Convers Manage* 2014;86:20–7.
- [17] Su L, Li X, He X, Liu F. Experimental research on the diffusion flame formation and combustion performance of forced swirl combustion system for DI diesel engines. *Energy Convers Manage* 2015;106:826–34.
- [18] Li X, Zhou H, Su L, Chen Y, Qiao Z, Liu F. Combustion and emission characteristics of a lateral swirl combustion system for DI diesel engines under low excess air ratio conditions. *Fuel* 2016;184:672–80.
- [19] Ng HK, Gan S, Ng J-H, Pang KM. Simulation of biodiesel combustion in a light-duty diesel engine using integrated compact biodiesel–diesel reaction mechanism. *Appl Energy* 2013;102:1275–87.
- [20] Yang Z, Chu C, Wang L, Huang Y. Effects of H_2 addition on combustion and exhaust emissions in a diesel engine. *Fuel* 2015;139:190–7.
- [21] Li X, Gao H, Zhao L, Zhang Z, He X, Liu F. Combustion and emission performance of a split injection diesel engine in a double swirl combustion system. *Energy* 2016;114:1135–46.
- [22] Wen X, Luo Y, Luo K, Jin H, Fan J. LES of pulverized coal combustion with a multi-regime flamelet model. *Fuel* 2017;188:661–71.
- [23] Musu E, Rossi R, Gentili R, Reitz RD. Heavy duty HCPC. SAE paper 2011-01-1824; 2011.
- [24] Komiyama K, Heywood JB. Predicting NOx emissions and effects of exhaust gas recirculation in spark-ignition engines. SAE paper 730475; 1973.
- [25] Li X, Sun Z, Liu F, Bai B. Research on parametric design of double swirl combustion chamber. In: International conference on computer distributed control and intelligent environmental monitoring. 2011:251–8.
- [26] Wei S, Ji K, Leng X, Wang F, Liu X. Numerical simulation on effects of spray angle in a swirl chamber combustion system of DI (direct injection) diesel engines. *Energy* 2014;75:289–94.
- [27] Li X-R, Yang W, Su L-W, Liu F-S. Mixing and combustion mechanisms within lateral swirl combustion system (LSCS) in a DI diesel engine. *Appl Therm Eng* 2017;123:7–18.
- [28] Gao H, Li X, Xue J, Bai H, He X, Liu F. Sensitivity analysis on the effect of background temperatures and densities on the diesel spray characteristics. *J Harbin Eng*

- Univ 2016;37(11):1553–9.
- [29] Yong S, Liu FS, Xiang-Rong LI, Wei DU. Research on the effect of forced swirl combustion chamber on air-fuel mixture process in diesel engine. *Trans Csice* 2010;28(6):488–93.
- [30] Li X, Sun Z, Du W, Wei R. Research and development of double swirl combustion system for a DI diesel engine. *Combust Sci Technol* 2010;182(8):1029–49.
- [31] Su L, Li X, Li J, Zhao L, Zhang C, Liu F. Experiment of emissions characteristics for double swirl combustion system in diesel engine. *Trans Chin Soc Agric Eng* 2013;29(21):60–5.